CHEMISTRY

Infrared vibrational nano-crystallography and nano-imaging

Eric A. Muller,[1] Benjamin Pollard,[1] Hans A. Bechtel,[2] Peter van Blerkom,[1] Markus B. Raschke[1]*

Molecular solids and polymers can form low-symmetry crystal structures that exhibit anisotropic electron and ion mobility in engineered devices or biological systems. The distribution of molecular orientation and disorder then controls the macroscopic material response, yet it is difficult to image with conventional techniques on the nanoscale. We demonstrated a new form of optical nano-crystallography that combines scattering-type scanning near-field optical microscopy with both optical antenna and tip-selective infrared vibrational spectroscopy. From the symmetry-selective probing of molecular bond orientation with nanometer spatial resolution, we determined crystalline phases and orientation in aggregates and films of the organic electronic material perylenetetracarboxylic dianhydride. Mapping disorder within and between individual nanoscale domains, the correlative hybrid imaging of nanoscale heterogeneity provides insight into defect formation and propagation during growth in functional molecular solids.

INTRODUCTION

Heterogeneous molecular spatial distribution, morphology, and structure define coupling and photophysical properties of organic electronic materials and biological systems. Directional bonding and intermolecular interactions lead to anisotropic ion, electron, and hole mobilities. In molecular devices, charge mobility is typically confined to one or two dimensions and has a high sensitivity to crystallinity, defects, and nanoscale orientation. Mobility enhancements of over two orders of magnitude have been demonstrated by, for example, improving long-range orientational ordering in spin-cast conductive polymers (1, 2) and engineering oriented growth of crystals within field-effect transistors and organic light-emitting diodes (3, 4).

Optical crystallography measures crystal axis orientation through the anisotropic response of electronic or vibrational modes on the basis of the projection of transition dipoles along the electric field vectors of incident radiation (5). However, complex soft matter has significant heterogeneity on the nanometer length scale, and conventional techniques typically measure only a diffraction-limited response that is spatially averaged over a large sample area.

Superresolution methods can determine molecular orientation in materials but require suitable optical response or exogenous fluorescent probes (6–8). High-spatial resolution crystallography is, in principle, possible using electron or x-ray methods, but restrictions abound because of the low-scattering cross section of organic materials, requirements for sufficient crystallinity, special sample preparation requirements, and sample damage (9–12).

Vibrational spectroscopy can be used for nondestructive optical crystallography across a wide range of inorganic, organic, and biological systems, additionally providing information on crystalline phase, chemical identity, and local chemical environment (13–16). Selective probing of characteristic vibrational modes can directly measure molecular orientation and crystallinity. Infrared (IR) optical crystallography uses an anisotropic material response proportional to the projection of vibrational transition dipole. Symmetry selectivity is achieved through choice of polarization and **k** vector of incident and emitted radiation, although it is limited in momentum space compared to x-ray techniques and optical spatial resolution. Here, we use scattering-type scanning near-field optical microscopy (s-SNOM) with combined tip- and vibrational-mode polarization and spectral selectivity for optical nano-crystallography, as shown in Fig. 1A. In s-SNOM, the metallized tip of an atomic force microscope (AFM) localizes and enhances the optical field linearly polarized parallel with respect to the tip axis. The resulting anisotropic linear and nonlinear optical response of the coupled tip and sample has already been applied to phonon selection rules in solids and broken symmetries in ferroelectrics (17–19).

We extended this approach to IR nano-crystallography of molecular and soft matter using linearly polarized near-field excitation with selection rules for vibrational modes, simultaneously providing chemical and polymorph identification and mapping heterogeneity in the local environment. We measured crystalline orientation with subdomain spatial resolution in films and aggregates of the molecular semiconductor perylenetetracarboxylic dianhydride (PTCDA). We performed hybrid correlative imaging by combining optical and topographic information to determine the characteristic length scales of order. We observed orientational defects with implications toward understanding growth mechanisms and enabling directed design of molecular devices.

PTCDA has attracted interest in organic electronics because of its high charge carrier mobility, crystallinity, and chemical stability (20). Good device performance can be obtained from high-purity thin films with well-ordered morphology and large crystalline domains, typically forming in one of two polymorphs, α or β, with both monoclinic structures containing stacked sheets of PTCDA arranged in a herringbone pattern, as shown in Fig. 1B. However, the charge carrier mobility of PTCDA is anisotropic and is significantly higher along the direction of π stacking (21). Even in devices with high crystallinity and micrometer grain size, misorientation of crystalline domains with respect to larger device architecture can decrease performance (3, 22).

In vacuum-deposited films, PTCDA crystals can be grown with the *a* axis oriented along the surface normal, favoring π stacking (Fig. 1C). However, the morphology is sensitive to growth conditions (23–25), substrate interactions (26), surface polymorphs distinct from the bulk phase (27, 28), minority phases (29), and defects. Although the structure

[1]Department of Physics, Department of Chemistry, and JILA, University of Colorado, Boulder, CO 80309, USA. [2]Advanced Light Source Division, Lawrence Berkeley National Laboratory, Berkeley, CA 94720, USA.
*Corresponding author. Email: markus.raschke@colorado.edu

in PTCDA and related molecular materials has been investigated at length scales ranging from molecular adsorption conformation to ensemble-averaged crystallinity, a unified understanding of defects and domain structure remains elusive.

EXPERIMENT

We used the combination of both narrowband IR *s*-SNOM based on tunable QCLs and broadband synchrotron IR nanospectroscopy (SINS) (*19*, *30*, *31*). Figure 1A shows the IR *s*-SNOM setup. Polarized IR light from a tunable laser or synchrotron is focused onto a metallized AFM tip operated in intermittent contact mode (see Materials and Methods). Tip-scattered near-field signal is combined with light from a reference arm and interferometrically amplified and detected, measuring the complete IR optical response through the frequency-dependent optical amplitude $A_{NF}(\bar{\nu})$ and phase $\Phi_{NF}(\bar{\nu})$ (*31*–*33*).

The frequency-dependent optical response for linearly polarized near-field excitation of characteristic modes with known transition dipoles is a general measure of molecular orientation relative to the *s*-SNOM tip and substrate. We implemented tip-enhanced IR optical nano-crystallography by selectively detecting only the material response along the tip axis, combining vertically polarized incident light, anisotropic field enhancement by the tip, and surface optical selection rules to measure the projection of vibrational dipoles along the tip axis. The selected orthogonal vibrational normal modes we probed have transition dipoles parallel to the primary molecular axes, thus reflecting the crystal axes for monoclinic PTCDA crystals (for details, see the Supplementary Materials).

Figure 1 (C and D) shows the AFM topography of drop-cast PTCDA aggregates and vacuum-deposited films, respectively. AFM topography across the surface shows well-separated regions containing clusters of PTCDA with a typical grain size in the range of 0.5 to 2 μm. The AFM height image of vacuum-deposited films in Fig. 1D shows islands with an average height of ~80 nm relative to the Au substrate. Island growth is observed by AFM tapping phase imaging, which identifies the islands and the spacing between them via differences in the tapping phase (see the Supplementary Materials) (*34*, *35*). The topography is consistent with previous observations of PTCDA films grown under similar conditions, producing a modified Stranski-Krastanov growth and appearing as three-dimensional (3D) islands for films greater than a few nanometers thick.

RESULTS

Figure 2A shows far-field Fourier transform IR spectroscopy (FTIR) spectra of PTCDA crystallites over two spectral regions of interest, 700 to 900 cm⁻¹ and 1600 to 1900 cm⁻¹, with the full spectra shown in the Supplementary Materials. The low-wavenumber region contains three prominent peaks assigned to C–H out-of-plane bending modes, whereas the carbonyl stretching region contains four overlapping peaks assigned to the anhydride groups. The anhydride modes are split into four peaks in the carbonyl region due to dipole-dipole coupling (*36*). Although broad line shapes prevent distinguishing between α and β
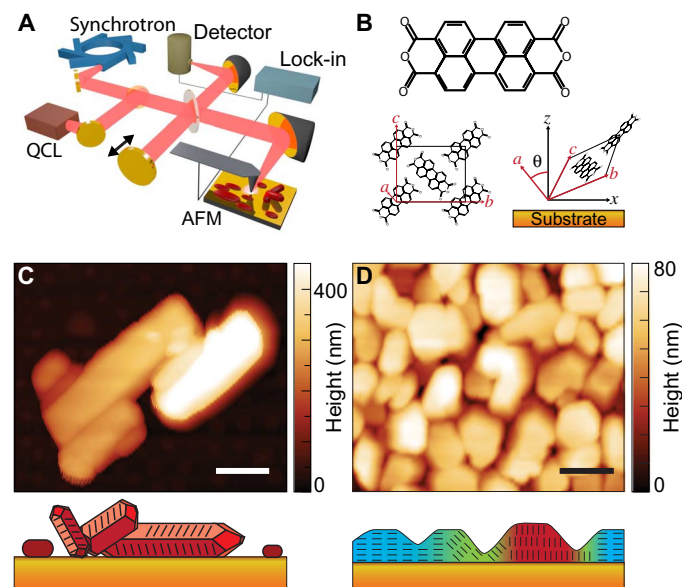
Fig. 1. IR nano-crystallography. (A) Schematic of IR *s*-SNOM using both synchrotron and quantum cascade laser (QCL) radiation. **(B)** Lewis structure (top) and crystal structure (bottom) of PTCDA in the β phase. (Bottom right) Crystal axes (red) oriented relative to the substrate, with θ indicating the angle between the *a* axis of the crystal and the *z* axis of the surface normal. **(C)** AFM height of aggregates, depicted schematically (bottom). Scale bar, 500 nm. **(D)** AFM height of vacuum-deposited film, with schematic (bottom) showing growth of molecules with the *a* axis parallel to the *z* axis (blue) and defects with the *a* axis perpendicular to the *z* axis (red and green). Scale bar, 200 nm.
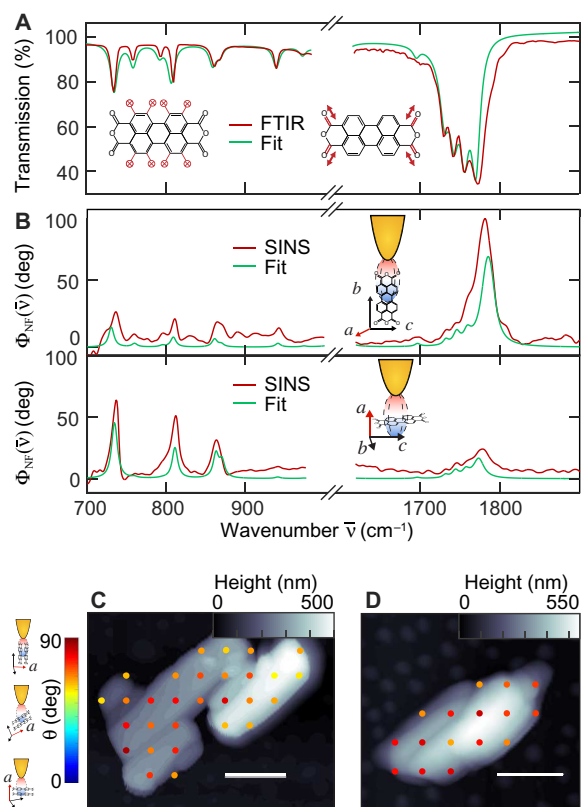
Fig. 2. Broadband IR *s*-SNOM of large crystallites. (A) Far-field transmission spectrum of dispersed PTCDA particles, fit to calculated reflectance using the Lorentz model. Inset: Schematic of C–H out-of-plane vibrations and C=O stretch of the anhydride. **(B)** SINS spectra (red) collected at two different nanoscale locations with (green) fit to spherical dipole model with Lorentz oscillators. **(C and D)** Molecular orientation is measured from SINS spectra in a spatial map across large crystals of PTCDA. Point spectra (circles) show fits of point spectra for θ, represented on a false-color scale. Scale bars, 500 nm.

phases, the splitting is consistent with the typical herringbone crystal structure and indicates high crystallinity of the powdered sample (*37*).

We fit the far-field transmission spectrum to quantify the peak position and oscillator strength (see the Supplementary Materials). The measured transmission of each peak is proportional to the vibrational oscillator strength for an ensemble measurement of isotropically dispersed particles. We found good agreement between measured and previously reported oscillator strengths (*37*).

Figure 2B shows SINS point spectra of $\Phi_{NF}(\bar{v})$ collected from different drop-cast PTCDA crystallites. As in the far-field spectrum (Fig. 2A), three C–H bending modes are observed in the low-frequency region, and four C=O stretching modes appear in the high-frequency region. The C–H and C=O modes alternate in peak height in *s*-SNOM spectra from different spatial regions containing subensembles with distinct orientations. Whereas the far-field spectra represent an isotropic ensemble-averaged sample response, near-field Φ_{NF} (C–H) and Φ_{NF} (C=O) measure anisotropic linear dichroism of an oriented nanoscale subensemble.

To determine the local crystallographic orientation, we calculated the near-field optical response of the coupled tip and sample system. The frequency-dependent IR dielectric constant $\epsilon(\bar{v})$ of PTCDA can be expressed as the sum of individual molecular vibrations using a Lorentz model for vibrational oscillators. The transition dipole of the C–H modes is parallel to the *a* axis, whereas the transition dipole of the C=O modes is along the $b − c$ plane of monoclinic PTCDA crystals and nearly isotropic in two dimensions. We include the Lorentz oscillator model in the well-known spherical-dipole model for near-field scattering (see the Supplementary Materials), which approximates the AFM tip as a polarizable sphere (*38–41*). The optical near-field maintains the polarization of incident light oriented parallel to or perpendicular to the tip axis (*42*), particularly in the strongly localized and enhanced region at the tip apex that dominates the signal. We then used the combined Lorentz oscillator and spherical dipole model to quantitatively calculate the IR *s*-SNOM signal as a function of molecular and crystalline orientation.

Figure 2B also shows the resulting fits of the model to the *s*-SNOM scattered signal from two representative PTCDA crystallites. The measured spectra quantify the projection of each mode along the tip axis and are insensitive to molecular rotation about the tip axis. We fit each spectrum to determine the projection angle θ of the crystalline *a* axis along the surface normal *z*, as shown in Fig. 1B. The angle θ is the only free fit parameter, whereas the oscillator strength and line widths of each normal mode are left as constants. The resulting values for θ in Fig. 2B are 70 ± 10° and 20 ± 10°, respectively.

From repeated measurements on a spatial grid and analysis from above, Fig. 2 (C and D) shows the molecular orientation measured across two PTCDA crystallites. Color scale indicates the orientation at each location in the image, with blue corresponding to θ = 0° and red corresponding to θ = 90°, with the *a* axis parallel to the substrate. These spectrally resolved maps identify large oriented regions with the *a* axis nearly parallel to the substrate across micrometer-sized crystallites and preferentially ordered in stacked aggregates. The spectral features and orientation-dependent enhancement are also consistent across all vibrational modes in the spectral range of SINS measurements (700 to 900 cm^{-1}) and are relatively insensitive to topographic variations or eigenmodes appearing due to sample geometry. Measured angles of θ = 60° to 90° across most of the crystallite demonstrate quantitative and robust measurement of orientation.

We extended the IR optical nano-crystallography to high-resolution single-wavelength imaging of orientational ordering in device-relevant thin films. Near-field $\Phi_{NF}(\bar{v})$ quantitatively measures the orientation θ by the relative contribution of C–H versus C=O peaks. Close agreement between calculated fits and broadband SINS spectra across all modes in PTCDA aggregates with different orientation establishes that Φ_{NF} at a selected frequency resonant with only one mode can be used to determine θ in the case of polycrystalline molecular semiconductors with uniform density. Further, near-field $\Phi_{NF}(\bar{v})$ is also independent of laser intensity, enabling quantitative comparison between measurements using different IR sources.

Figure 3A shows the AFM topography at the edge of a vacuum-deposited ~80-nm-thick film with the expected morphology of 3D islands across most of the continuous films. Figure 3B shows the corresponding *s*-SNOM imaging resonant with the carbonyl mode at 1777 cm^{-1}, Φ_{NF} (C=O). Φ_{NF} (C=O) measures the projection of the C=O transition dipole along the tip axis. The resonant Φ_{NF} (C=O) image shows significant spatial variation and several distinct regions across the image, as opposed to Φ_{NF} at nonresonant frequencies, which shows no optical contrast across the sample (see the Supplementary Materials).

Several distinct regions are seen in the Φ_{NF} (C=O) image. The Au substrate is nonresonant and serves as a reference region, with Φ_{NF} (C=O) near 0°, whereas Φ_{NF} (C=O) = 10° to 30° is observed across most of the PTCDA. Near the film edge, regions with Φ_{NF} (C=O) ≥ 70° are observed. Comparing the resonant $\Phi_{NF}(\bar{v})$ across the PTCDA to the calculated *s*-SNOM signal with the spherical dipole model, we can assign the orientation distribution across most of the sample area. Away from the edge, θ ≤ 20°, whereas the region of higher $\Phi_{NF}(\bar{v})$ corresponds to a larger θ = 50 ± 10°, with uncertainties calculated from the 95% confidence limit of Φ_{NF}.

Correlation analysis (Fig. 3C) of topography and Φ_{NF} (C=O) provides for assignment of spatial regions with distinct crystal orientation. Regions of lowest height also have Φ_{NF} (C=O) ~ 0°, indicating nonresonant response, which can be assigned to the exposed Au substrate. Higher topography corresponds to the thin film with 3D islands. Most of the population of PTCDA regions has a low measured Φ_{NF} (C=O) and θ, whereas smaller populations are observed to exhibit a larger Φ_{NF} (C=O) and θ.

Figure 3D shows the resulting orientational map. Most of the image (green) has a height near the average film thickness and θ = 10° to 20° measured by Φ_{NF} (C=O). However, near the edge, a region is perturbed with both higher topography and greater θ (red). Although much of the uplifted region near the edge has greater θ, one of the tallest island features (light blue) exhibits low θ, similar to the response of the unperturbed region (green). At the edge of the PTCDA region, a small region (yellow) of low height yet with large θ is also observed as a spatially distinct subensemble that is unobservable from either height or θ alone.

We next analyzed a small region of PTCDA in a central region of the overall film to study the intrinsic heterogeneity in the vacuum-deposited film. Figure 4 (A and B) shows a high-resolution AFM and *s*-SNOM image of a small region containing the orientational defects. The AFM height shows morphological features associated with the 3D island growth of PTCDA. The Φ_{NF} (C=O) image that is resonant with the carbonyl mode shows that, across most of the image, the molecular orientation is relatively flat, as expected for vacuum-deposited growth on Au. Across most of the image, a weak correlation is observed between features observed in AFM height and in Φ_{NF} (C=O), whereas, in two distinct regions with higher Φ_{NF} (C=O) (Fig. 4B), the *a* axis is oriented significantly away from the surface
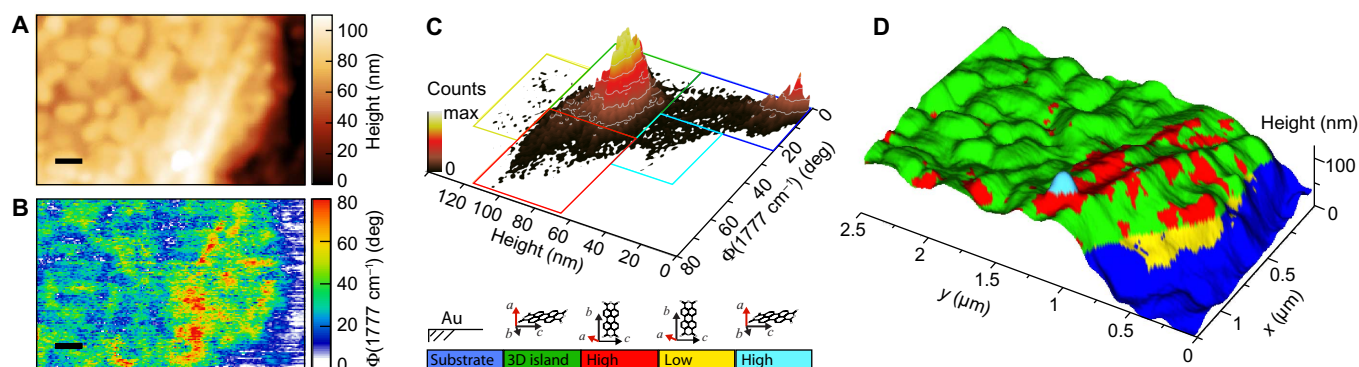
Fig. 3. Correlative analysis of defects. AFM topography of vacuum-deposited PTCDA near the film edge (**A**) and corresponding near-field Φ_{NF} (1777 cm^{-1}) measured on resonance with the carbonyl mode (**B**). Scale bars, 500 nm. (**C**) Histogram constructed from the images (A and B) showing correlation between AFM height and Φ_{NF} (1777 cm^{-1}). Distinct subpopulations are identified by their statistical correlation and labeled by the colored borders. (**D**) Spatial map reconstructed from the correlated populations identified in (C) overlaid on AFM height image. Most of the population (green) has the *a* axis of PTCDA parallel to the surface normal, with smaller populations uplifted with the *a* axis parallel to the surface normal (light blue), uplifted regions with the *a* axis oriented away from the surface normal (red), and regions with less coverage and *a* axis oriented away from the surface normal (yellow). The substrate is shaded dark blue.

normal. In particular, the defect in the lower right portion of the image has a maximum Φ_{NF} (C=O) of 85° localized to a region of ~100 nm as well as an extended region with Φ_{NF} (C=O) near 45°. From the corresponding line scan (Fig. 4C) of the location indicated by the dotted lines in Fig. 4 (A and B), we observed regions of high Φ_{NF} (C=O) in regions with both low and high topography. Spatial variations in Φ_{NF} (C=O) appear uncorrelated with height and extend across and beyond the edge of the 3D islands.

Figure 4D shows the radial correlation functions from AFM and Φ_{NF} (C=O) signals. We analyzed the AFM tapping phase, which was found to be a sensitive measure of islands and the regions between islands, which may be due to differences in sample viscoelasticity, adsorbed water, or geometrical effects (*34*, *35*). Periodicity in the AFM tapping phase signals indicates well-separated island features with 200-nm spacing, as measured by the location of the first maximum in the radial correlation function. However, the radial correlation function of the optical phase decays monotonically with no periodic recurrence of correlation, supporting the finding that the observed θ is uncorrelated with the morphological features or edge effects. Further, the correlation length Φ_{NF} (C=O) is comparable to or greater than the spacing of morphological features. The long radial correlation of the Φ_{NF} (C=O) agrees with the conclusions from the line scan in Fig. 4C and supports the idea that the orientational defects are not confined within a single morphological feature and may, in fact, extend across multiple island features.

DISCUSSION

Our IR *s*-SNOM optical nano-crystallography and nano-imaging show the presence of well-oriented PTCDA in macroscopically disordered drop-cast crystallites. Conversely, vacuum-deposited PTCDA is macroscopically ordered in the crystalline thin film, with molecules primarily oriented with θ ≃ 10° to 20°, in close agreement with previous ensemble-averaged measurements (*26*). However, we found nanoscale spatial variation of molecular orientation in otherwise morphologically well-ordered regions of the vacuum-deposited thin film. Line scans and correlation analysis of Φ_{NF} (C=O) suggest that defects and crystalline domains may not be confined to individual morphological features.
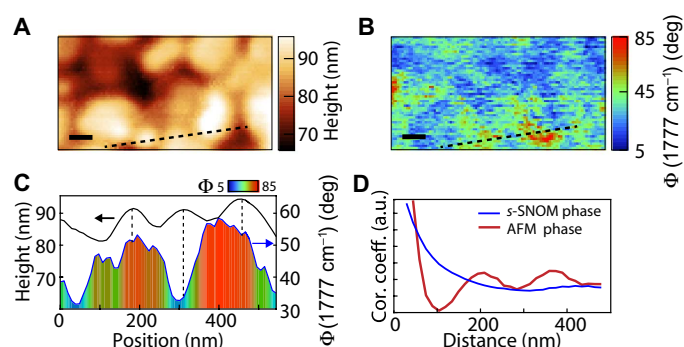
Fig. 4. Subdomain nanoscale orientation. Topography (**A**) and Φ_{NF} (C=O) images (**B**) of PTCDA. Scale bars, 100 nm. (**C**) Line cut of AFM height and $\Phi(\bar{\nu})$ along the dashed transect indicated in (A) and (B), showing that molecular orientation is uncorrelated with topographic features. (**D**) Radial correlation function (red) of the AFM tapping phase, indicating the presence of 3D islands with characteristic size and spacing and $\Phi(\bar{\nu})$ (blue), which shows an extended correlation length of crystallite orientation. Cor. coeff., correlation coefficient; a.u., arbitrary units.

The observed orientational radial correlation length across the PTCDA sample can be expected to occur during growth by vacuum deposition. Thin-film growth of different morphologies with varying crystallinity, polymorphs, and even amorphous growth can occur as a function of growth rate and temperature. Roughness of the substrate may also play a role, which, for our template-stripped Au, has a measured root mean square roughness of 0.5 nm, yet with many features as high as 5 nm and rare pit defects. Defect propagation during vacuum deposition is expected to be influenced by both the density of seed crystals and the molecular surface diffusion rate across morphological features.

IR vibrational nano-crystallography extends related tip-enhanced nanoscale crystallography efforts to molecular materials. Imaging orientation of inorganic crystals has been demonstrated via IR *s*-SNOM using crystallographic anisotropy of the phonon response (*17*), although quantitative determination of orientation angle and structural information were inaccessible. Symmetry selectivity of nonlinear response has also been used to image domain order in ferroelectrics (*18*).

The polarizability tensor has also been used in tip-enhanced Raman spectroscopy to measure orientation of inorganic microcrystals (19).

With the combination of selected wavelength imaging and broadband IR spectroscopy, the approach of s-SNOM–based optical crystallography can be generalized and extended to a much wider range of materials. The low photon energy of IR light and lower-field enhancement in IR s-SNOM provide minimally invasive imaging, suitable for organic materials even under ambient and device-relevant conditions. Individual-wavelength IR s-SNOM enables rapid imaging of $\Phi_{NF}(\bar{v})$ simultaneously with AFM information under the conditions of spatially invariant chemical identity and density. These methods can be expanded to image more complex and multicomponent materials. IR s-SNOM nano-crystallography measured using both horizontal and vertical polarized optical fields can measure molecular orientation through linear dichroism of a single vibrational mode even with varying molecular concentration and oscillator density. Hyperspectral imaging of several vibrational modes with different point group symmetries can uniquely reflect molecular orientation while also measuring chemical identity.

Broadband IR–nano-crystallography based on hyperspectral imaging can be improved with faster spectral acquisition times using sources of adequate average power and a carefully selected frequency bandwidth. By overcoming these technical limitations, our methods and analysis are generalizable to imaging orientational heterogeneity in virtually any soft matter, multicomponent, or partially ordered system.

CONCLUSIONS

In summary, we implemented IR s-SNOM for optical nano-crystallography using tip-enhanced spectroscopy of molecular vibrations with IR selection to quantify the molecular and crystalline orientation while providing simultaneous spectral sensitivity for chemical identification and measurement of crystalline phases and variation in the local chemical environment. We measured the heterogeneity of polycrystalline PTCDA on the natural length scales of disorder, including orientation distribution and correlation across domain boundaries and morphological features. We observed both the correlation between nanoscale crystallinity and associated morphological features and the local variation in molecular orientation that is uncorrelated with morphological features. We directly measured the molecular-level structure and interactions that govern macroscopic properties, adding unique insight into crystalline growth and defect propagation in device-relevant films.

MATERIALS AND METHODS

In the IR s-SNOM apparatus, light from a tunable laser or synchrotron radiation was focused onto a metallized AFM tip operated in intermittent contact mode $v_0 \sim 250$ kHz. Near-field signal was detected at a higher harmonic of the tapping frequency using lock-in demodulation. In both continuous-wave and broadband implementations, the tip-scattered near-field signal was combined with light from a reference arm and interferometrically detected with a HgCdTe photovoltaic detector.

SINS was performed using a Bruker Innova AFM modified for s-SNOM. Point spectra were measured interferometrically with a modified FTIR (Nicolet 6700), which was collected as asymmetric interferograms. Interferograms were Fourier-transformed to produce near-field $A_{NF}(\bar{v})$ and $\Phi_{NF}(\bar{v})$ spectra. A single interferogram at 8 cm^{-1} was collected within 2 s, and spectra were averaged over typically 60 to 1000 repeated scans and referenced to a nonresonant bare Au substrate. For spatially resolved spectroscopic imaging, faster resolution imaging was performed at a lower resolution of 16 cm^{-1}.

Selected, fixed-wavelength imaging was performed using a tunable QCL (Daylight Solutions Inc.) with an Anasys nanoIR2-s AFM. Fixed-wavelength imaging within the range (1650 to 1850 cm^{-1}) measures $A_{NF}(\bar{v})$ and $\Phi_{NF}(\bar{v})$ simultaneously with AFM topographic information.

PTCDA films and aggregates were prepared from sublimation-purified ≥99% pure powder (Sigma-Aldrich). Transition dipole strength of vibrational modes was determined from FTIR of crystallites dispersed in KBr powder, with similar results observed for drop-cast crystallites. Aggregated crystallite samples were prepared drop-cast from a low-solubility suspension in dichloromethane solvent on substrates of freshly prepared template-stripped Au substrates with a root mean square roughness of 0.5 nm. Vacuum-deposited films were prepared by organic molecular beam deposition from a Knudsen cell held at 630 K at a rate of ~2 nm/min, producing films with a nominal thickness of 80 nm.

Film morphology was characterized with tapping-mode AFM, and far-field FTIR spectra were collected in transmission mode (Nicolet 6700; 2-cm^{-1} resolution) as well as a far-field transmission and reflectance FTIR microscope (Continuum) with numerical aperture of 0.65 using a 50-μm × 50-μm aperture.

SUPPLEMENTARY MATERIALS

Supplementary material for this article is available at http://advances.sciencemag.org/cgi/content/full/2/10/e1601006/DC1

Description of modeling and calculations for IR vibrational nano-crystallography
Description of nonresonant signal and signal penetration depth
fig. S1. Experiment and calculated near- and far-field spectra.
fig. S2. Orientation dependence of near-field signal.
fig. S3. Nonresonant near-field signal.

REFERENCES AND NOTES

1. C. Luo, A. K. K. Kyaw, L. A. Perez, S. Patel, M. Wang, B. Grimm, G. C. Bazan, E. J. Kramer, A. J. Heeger, General strategy for self-assembly of highly oriented nanocrystalline semiconducting polymers with high mobility. *Nano Lett.* **14**, 2764–2771 (2014).
2. H.-R. Tseng, H. Phan, C. Luo, M. Wang, L. A. Perez, S. N. Patel, L. Ying, E. J. Kramer, T.-Q. Nguyen, G. C. Bazan, A. J. Heeger, High-mobility field-effect transistors fabricated with macroscopic aligned semiconducting polymers. *Adv. Mater.* **26**, 2993–2998 (2014).
3. J. Rivnay, L. H. Jimison, J. E. Northrup, M. F. Toney, R. Noriega, S. Lu, T. J. Marks, A. Facchetti, A. Salleo, Large modulation of carrier transport by grain-boundary molecular packing and microstructure in organic thin films. *Nat. Mater.* **8**, 952–958 (2009).
4. D. Yokoyama, H. Sasabe, Y. Furukawa, C. Adachi, J. Kido, Molecular stacking induced by intermolecular C–H···N hydrogen bonds leading to high carrier mobility in vacuum-deposited organic films. *Adv. Funct. Mater.* **21**, 1375–1382 (2011).
5. L. Wong, C. Hu, R. Paradise, Z. Zhu, A. Shtukenberg, B. Kahr, Relationship between tribology and optics in thin films of mechanically oriented nanocrystals. *J. Am. Chem. Soc.* **134**, 12245–12251 (2012).
6. A. M. Chizhik, S. Stein, M. O. Dekaliuk, C. Battle, W. Li, A. Huss, M. Platen, I. A. T. Schaap, I. Gregor, A. P. Demchenko, C. F. Schmidt, J. Enderlein, A. I. Chizhik, Super-resolution optical fluctuation bio-imaging with dual-color carbon nanodots. *Nano Lett.* **16**, 237–242 (2016).
7. R. H. Goldsmith, W. E. Moerner, Watching conformational- and photodynamics of single fluorescent proteins in solution. *Nat. Chem.* **2**, 179–186 (2010).
8. C. Y. Wong, B. D. Folie, B. L. Cotts, N. S. Ginsberg, Discerning variable extents of interdomain orientational and structural heterogeneity in solution-cast polycrystalline organic semiconductors thin films. *J. Phys. Chem. Lett.* **6**, 3155–3162 (2015).
9. P. Thibault, M. Dierolf, A. Menzel, O. Bunk, C. David, F. Pfeiffer, High-resolution scanning x-ray diffraction microscopy. *Science* **321**, 379–382 (2008).
10. G. F. Schröder, M. Levitt, A. T. Brunger, Super-resolution biomolecular crystallography with low-resolution data. *Nature* **464**, 1218–1222 (2010).
11. D. M. DeLongchamp, R. J. Kline, A. Herzing, Nanoscale structure measurements for polymer-fullerene photovoltaics. *Energy Environ. Sci.* **5**, 5980–5993 (2012).
12. B. A. Collins, J. E. Cochran, H. Yan, E. Gann, C. Hub, R. Fink, C. Wang, T. Schuettfort, C. R. McNeill, M. L. Chabinyc, H. Ade, Polarized X-ray scattering reveals non-crystalline orientational ordering in organic films. *Nat. Mater.* **11**, 536–543 (2012).

13. D. S. Miller, R. J. Carlton, P. C. Mushenheim, N. L. Abbott, Introduction to optical methods for characterizing liquid crystals at interfaces. *Langmuir* **29**, 3154–3169 (2013).

14. A. Chandran, A. Choudhary, P. Singh, D. Haranath, A. M. Biradar, Probing the dynamics of geometrically confined ferroelectric mesogens at the air interface. *Soft Matter* **11**, 749–755 (2015).

15. B. Bechinger, J.-M. Ruysschaert, E. Goormaghtigh, Membrane helix orientation from linear dichroism of infrared attenuated total reflection spectra. *Biophys. J.* **76**, 552–563 (1999).

16. C. Yuan, J. Zhang, G. Chen, J. Yang, Insight into carbon nanotube effect on polymer molecular orientation: An infrared dichroism study. *Chem. Commun.* **47**, 899–901 (2011).

17. S. C. Kehr, M. Cebula, O. Mieth, T. Härtling, J. Seidel, S. Grafström, L. M. Eng, S. Winnerl, D. Stehr, M. Helm, Anisotropy contrast in phonon-enhanced apertureless near-field microscopy using a free-electron laser. *Phys. Rev. Lett.* **100**, 256403 (2008).

18. C. C. Neacsu, B. B. van Aken, M. Fiebig, M. B. Raschke, Second-harmonic near-field imaging of ferroelectric domain structure of YMnO₃. *Phys. Rev. B* **79**, 100107(R) (2009).

19. S. Berweger, C. C. Neacsu, Y. Mao, H. Zhou, S. S. Wong, M. B. Raschke, Optical nanocrystallography with tip-enhanced phonon Raman spectroscopy. *Nat. Nanotechnol.* **4**, 496–499 (2009).

20. L.-N. Nguyen, S. Kumar Pradhan, C.-N. Yen, M.-C. Lin, C.-H. Chen, C.-S. Wu, K.-S. Chang-Liao, M.-T. Lin, C.-D. Chen, High performance phototransistors based on single crystalline perylene-tetracarboxylic-dianhydride nanoparticle. *Appl. Phys. Lett.* **103**, 183301 (2013).

21. A. L. Briseno, S. C. B. Mannsfeld, M. M. Ling, S. Liu, R. J. Tseng, C. Reese, M. E. Roberts, Y. Yang, F. Wudl, Z. Bao, Patterning organic single-crystal transistor arrays. *Nature* **444**, 913–917 (2006).

22. A. Lv, S. R. Puniredd, J. Zhang, Z. Li, H. Zhu, W. Jiang, H. Dong, Y. He, L. Jiang, Y. Li, W. Pisula, Q. Meng, W. Hu, Z. Wang, High mobility, air stable, organic single crystal transistors of an n-type diperylene bisimide. *Adv. Mater.* **24**, 2626–2630 (2012).

23. F. Ciccullo, S.-A. Savu, A. Gerbi, M. Bauer, R. Ovsyannikov, A. Cassinese, T. Chassé, M. B. Casu, Chemisorption, morphology, and structure of a n-type perylene diimide derivative at the interface with gold: Influence on devices from thin films to single molecules. *Chemistry* **21**, 3766–3771 (2015).

24. K. Hänel, S. Söhnchen, S. Lukas, G. Beernink, A. Birkner, T. Strunskus, G. Witte, C. Wöll, Organic molecular-beam deposition of perylene on Cu(110): Results from near-edge x-ray absorption spectroscopy, x-ray photoelectron spectroscopy, and atomic force microscopy. *J. Mater. Res.* **19**, 2049–2056 (2011).

25. S. Lukas, S. Söhnchen, G. Witte, C. Wöll, Epitaxial growth of pentacene films on metal surfaces. *ChemPhysChem* **5**, 266–270 (2004).

26. S. Berger, K. Heimer, H. G. Mack, C. Ziegler, IR and SFM study of PTCDA thin films on different substrates. *Appl. Surf. Sci.* **252**, 81–84 (2005).

27. M. Willenbockel, D. Lüftner, B. Stadtmüller, G. Koller, C. Kumpf, S. Soubatch, P. Puschnig, M. G. Ramsey, F. S. Tautz, The interplay between interface structure, energy level alignment and chemical bonding strength at organic–metal interfaces. *Phys. Chem. Chem. Phys.* **17**, 1530–1548 (2015).

28. M. Marks, N. L. Zaitsev, B. Schmidt, C. H. Schwalb, A. Schöll, I. A. Nechaev, P. M. Echenique, E. V. Chulkov, U. Höfer, Energy shift and wave function overlap of metal-organic interface states. *Phys. Rev. B* **84**, 081301(R) (2011).

29. C. R. Braatz, T. Esat, C. Wagner, R. Temirov, F. S. Tautz, P. Jakob, Switching orientation of adsorbed molecules: Reverse domino on a metal surface. *Surf. Sci.* **643**, 98–107 (2016).

30. B. Pollard, E. A. Muller, K. Hinrichs, M. B. Raschke, Vibrational nano-spectroscopic imaging correlating structure with intermolecular coupling and dynamics. *Nat. Commun.* **5**, 3587 (2014).

31. H. A. Bechtel, E. A. Muller, R. L. Olmon, M. C. Martin, M. B. Raschke, Ultrabroadband infrared nanospectroscopic imaging. *Proc. Natl. Acad. Sci. U.S.A.* **111**, 7191–7196 (2014).

32. J. M. Atkin, P. M. Sass, P. E. Teichen, J. D. Eaves, M. B. Raschke, Nanoscale probing of dynamics in local molecular environments. *J. Phys. Chem. Lett.* **6**, 4616–4621 (2015).

33. E. A. Muller, B. Pollard, M. B. Raschke, Infrared chemical nano-imaging: Accessing structure, coupling, and dynamics on molecular length scales. *J. Phys. Chem. Lett.* **6**, 1275–1284 (2015).

34. A. Knoll, R. Magerle, G. Krausch, Tapping mode atomic force microscopy on polymers: Where is the true sample surface? *Macromolecules* **34**, 4159–4165 (2001).

35. L. Zitzler, S. Herminghaus, F. Mugele, Capillary forces in tapping mode atomic force microscopy. *Phys. Rev. B* **66**, 155436 (2002).

36. K. Akers, R. Aroca, A. M. Hor, R. O. Loutfy, Molecular organization in perylenetetracarboxylic dianhydride films. *J. Phys. Chem.* **91**, 2954–2959 (1987).

37. R. Scholz, M. Friedrich, G. Salvan, T. U. Kampen, D. R. T. Zahn, T. Frauenheim, Infrared spectroscopic study of the morphology of 3,4,9,10-perylene tetracarboxylic dianhydride films grown on H-passivated Si(111). *J. Phys. Condens. Matter* **15**, S2647–S2663 (2003).

38. T. Taubner, R. Hillenbrand, F. Keilmann, Nanoscale polymer recognition by spectral signature in scattering infrared near-field microscopy. *Appl. Phys. Lett.* **85**, 5064 (2004).

39. A. A. Govyadinov, I. Amenabar, F. Huth, P. S. Carney, R. Hillenbrand, Quantitative measurement of local infrared absorption and dielectric function with tip-enhanced near-field microscopy. *J. Phys. Chem. Lett.* **4**, 1526–1531 (2013).

40. A. S. McLeod, P. Kelly, M. D. Goldflam, Z. Gainsforth, A. J. Westphal, G. Dominguez, M. H. Thiemens, M. M. Fogler, D. N. Basov, Model for quantitative tip-enhanced spectroscopy and the extraction of nanoscale-resolved optical constants. *Phys. Rev. B* **90**, 085136 (2014).

41. S. Mastel, A. A. Govyadinov, T. V. A. G. de Oliveira, I. Amenabar, R. Hillenbrand, Nanoscale-resolved chemical identification of thin organic films using infrared near-field spectroscopy and standard Fourier transform infrared references. *Appl. Phys. Lett.* **106**, 023113 (2015).

42. T. Ishibashi, Y. Cai, Polarization properties in apertureless-type scanning near-field optical microscopy. *Nanoscale Res. Lett.* **10**, 375 (2015).

Science Advances

Infrared vibrational nanocrystallography and nanoimaging

Eric A. Muller, Benjamin Pollard, Hans A. Bechtel, Peter van Blerkom and Markus B. Raschke

ARTICLE TOOLS	http://advances.sciencemag.org/content/2/10/e1601006
SUPPLEMENTARY MATERIALS	http://advances.sciencemag.org/content/suppl/2016/10/03/2.10.e1601006.DC1
REFERENCES	This article cites 42 articles, 2 of which you can access for free http://advances.sciencemag.org/content/2/10/e1601006#BIBL
PERMISSIONS	http://www.sciencemag.org/help/reprints-and-permissions

Use of this article is subject to the Terms of Service